Duplexed CeTEAM drug biosensors reveal determinants of PARP inhibitor selectivity in cells

Maria J. Pires[1] , Seher Alam[1] , Alen Lovric[1] , Emanuele Fabbrizi[2], Dante Rotili[3,4], Mikael Altun[5,*] , and Nicholas C. K. Valerie[5,*]

From the [1]Division of Clinical Physiology, Department of Laboratory Medicine, Karolinska Institutet, Karolinska University Hospital; Huddinge, Sweden; [2]Department of Chemistry and Technology of Drugs, Sapienza University of Rome, Roma RM, Italy; [3]Department of Science, "Roma Tre" University, Rome, Italy; [4]INBB - Biostructures and Biosystems National Institute, Rome, Italy; [5]Science for Life Laboratory, Division of Clinical Physiology, Department of Laboratory Medicine, Karolinska Institutet, Karolinska University Hospital; Huddinge, Sweden.

Reviewed by members of the JBC Editorial Board. Edited by Karen Fleming

Poly (ADP-ribose) polymerase (PARP) inhibitors (PARPi) targeting PARP1 and PARP2 have revolutionized cancer therapy by selectively killing cancer cells with defective DNA repair. However, achieving PARP1 or PARP2-selective inhibitors is difficult due to structural homology. Selectivity profiling is typically done with purified proteins, but these lack the complexity of intracellular environments and could therefore be inaccurate. Here, we duplex PARP1 L713F-GFP and PARP2 L269A-mCherry cellular target engagement by accumulation of mutant (CeTEAM) drug biosensors to systematically characterize binding and cell cycle alterations of 27 PARPi. Our results reveal that most PARPi are equipotent for both PARPs, including the next-generation drug, senaparib. However, benzimidazole carboxamide (niraparib) derivatives demonstrated PARP1-selective tendencies, while phthalazinones (olaparib) favored PARP2. AZD5305, a reported PARP1-selective inhibitor with characteristics of both series, was the exception and appears ~1600-fold more potent toward PARP1. In agreement with current understanding, we see that trapping-associated S/G2-phase transitions positively correlate with PARP1/2 binding potency, while some potent binders, such as veliparib, did not – likely reflecting their allosteric influence on DNA retention. We also assessed the effect of the PARP1/2 active site component, histone PARylation factor 1, on intracellular PARPi binding and see that its depletion elicits slight deviations in apparent binding potency, while contributing additively to trapping-like phenotypes. The PARP1/2 CeTEAM platform thus provides a structural roadmap for the development of selective PARPi and should facilitate the discovery of targeted therapies. Furthermore, our results highlight that multiplexing CeTEAM biosensors and layered genetic perturbations can systematically profile determinants of intracellular drug selectivity.

PARP inhibitors (PARPi) have revolutionized treatment for cancers characterized by deficiencies in DNA repair mechanisms, particularly those involving mutations to the homologous recombination repair proteins, BRCA1 and BRCA2 (1). These drugs preferentially block the ability of PARP1 and PARP2 to initiate repair of DNA damage and selectively kill cancer cells that are unable to repair double strand breaks based on the concept of synthetic lethality (2, 3). This effect is further driven by the ability of some PARPi to trap PARP1 and PARP2 onto DNA, thereby creating more irreparable DNA damage (1, 4).

Most PARPi, consisting of a nicotinamide mimetic pharmacophore, indiscriminately target both PARP1 and PARP2 and, to a lesser extent, other PARP paralogs (4). Both PARPs have different N-terminal DNA binding domains but share homologous catalytic domains and allosteric regulatory mechanisms (5, 6). Therefore, specific targeting of their enzymatic activities has been challenging to date, despite differing allosteric outcomes in response to PARPi (5, 7). Nonetheless, each has unique biological functions warranting preferential targeting for therapeutic opportunities (8). For example, the hematological toxicity of current PARPi has been attributed to an on-target, adverse effect of PARP2 inhibition due to its essential role in erythroid progenitor differentiation (9, 10). Thus, despite an abundance of potent, clinical-grade inhibitors, the need for truly selective, next generation PARPi remains high.

Small molecule selectivity is traditionally assessed with purified proteins in vitro, as more exact calculations of the inhibitory potency and characterizations of the binding modality can be performed. However, selectivity profiling in cellular contexts, as opposed to with purified proteins, has unveiled disparities in inhibitor performance, underscoring that the cellular environment can significantly influence their behavior (11). For example, the interactions of PARP1 and PARP2 with cofactors like histone PARylation factor 1 (HPF1) can further complicate the pharmacodynamics of PARPi (12). HPF1 modulates the PARylation activity of PARP1 and PARP2 by effectively completing their enzymatic pockets, and, in turn, tuning their ability to interact with and modify histones during chromatin remodeling and DNA repair (12, 13). Thus, it is

* For correspondence: Nicholas C. K. Valerie, nicholas.valerie@ki.se; Mikael Altun, mikael.altun@ki.se.

reasonable to expect HPF1 to influence PARPi binding and activity. Indeed, early indications suggest that HPF1 can modulate PARPi binding potency *in vitro* (14, 15) and PARPi sensitivity *in cellulo* (16), but the effect on PARPi binding in cells has not been elucidated.

We recently introduced the cellular target engagement by accumulation of mutant (CeTEAM) assay, which leverages conditionally stabilized protein variants to monitor drug binding events in cells (17). These mutations cause the rapid degradation of the target protein unless stabilized by ligand binding, enabling a direct and dynamic measurement of drug-target engagement. Thus, a simple readout of drug biosensor abundance can be directly coupled to functional outcomes of tested small molecules to yield combined biophysical and phenotypic insights to drug action. Among the exemplified drug targets, we identified the PARP1 synthetic mutant, L713F, as a live-cell-compatible drug biosensor to contextualize PARPi binding and PARP trapping-like phenotypes. By structural homology profiling, we also identified that an analogous mutant of PARP2, L269A, could similarly be employed as a live-cell drug biosensor, implying that the suite of CeTEAM-compatible mutants can be rationally expanded.

Here, we utilize a duplexed, PARP1/2 CeTEAM biosensor platform to comprehensively profile the binding dynamics and S/G2-phase cell cycle perturbations of known PARPi in live cells. We also assess the influence of the PARP1/2 active site component, HPF1, on these readouts with RNAi. Our findings reveal potential structural determinants of PARPi selectivity toward PARP1 or PARP2 and provide a roadmap for integrating genetic screens into cell-based drug binding and selectivity assays. The multiplexed CeTEAM selectivity platform should be a valuable tool for evaluating the PARP1/2 binding and pharmacology of next-generation PARP inhibitors.

Results

Validation of a duplexed PARP1/2 CeTEAM fluorescent biosensor system

Despite almost all clinical PARPi targeting both PARP1 and PARP2, there is a paucity of data regarding intracellular PARP2 drug-target engagement, especially regarding relative potency (18–20). In our hands, we saw negligible shifts in endogenous PARP2 stability by the cellular thermal shift assay (CETSA), despite seeing expected increases in soluble PARP1 upon olaparib addition (21, 22), which may partially explain the limited data on PARP2 engagement in cells (Fig. S1, A–C). We previously demonstrated the CeTEAM amenability of GFP-tagged PARP1 L713F and the analogous mutant in PARP2 (L269A) individually with multiple PARPi by comprehensive concentration-response profiling (17).

To build a truly multiplexed platform for PARPi selectivity profiling, we utilized spectrally distinct fluorescent tags for simultaneous monitoring of PARP1 L713F (GFP) and PARP2 L269A (mCherry) within the same cellular context (Fig. 1). We validated this system by Western blot analysis after a 24-h PARPi treatment using talazoparib, olaparib, niraparib, veliparib, or 3-aminobenzamide (3-AB), with iniparib as a negative control

(Fig. 1, *A* and *B*). All PARPi showed concentration-dependent stabilization of PARP1 and PARP2 except for iniparib. As before (17), 3-AB required higher concentrations for similar engagement. Unexpectedly, niraparib stabilized PARP2 L269A significantly worse than PARP1 L713F at 1 μM. In line with differential scanning fluorimetry data for PARP1 L713F (17), we were able to orthogonally confirm PARPi binding to PARP1 L713F-GFP and PARP2 L269A-mCherry in cells by CETSA (Fig. S2, *A* and *B*). As with endogenous PARP2, there was a slight, but, in this case, distinguishable, increase in soluble protein after heat pulse. Notably, PARP1 L713F-GFP was already stabilized by PARPi at 37 °C, presumably reflecting the conditional stabilization of the CeTEAM mutant by a binding ligand.

PARPi concentration gradients by live-cell fluorescence microscopy confirmed the CeTEAM biosensor stabilization seen by Western blot and demonstrated essentially equipotent stabilization EC_{50} values with both biosensors, which ranged from ~2 nM (talazoparib) to ~300 to 500 μM (3-AB). These values were generally in close agreement with reported biochemical IC_{50} and K_i values (Fig. 1, *C–F*). Notably, however, niraparib binding to PARP2 L269A-mCherry was worse by > 10-fold (~11 nM *versus* ~133 nM) (23). Findings with L269A-mCherry were consistent with earlier stabilization EC_{50} values from PARP2 L269A-GFP (17), suggesting that the choice of fluorescent protein tag did not specifically contribute to observed stabilization changes (Fig. 1*F*). Thus, our PARP1/2 duplexed CeTEAM biosensor system is a capable platform for detailed pharmacological assessments of PARP inhibitors.

Rescreening of PARP1 L713F-nLuc stabilizers with the PARP1/2 CeTEAM assay

We previously screened a ~1200 compound drug-like library for PARP1 L713F biophysical perturbagens and found >90% of potent PARP1i, as well as several non-PARPi that also stabilized the nLuc biosensor (17). To determine if these molecules also affected PARP2 L269A stability, we then rescreened the original hits with the duplexed PARP1/2 CeTEAM assay (Fig. 2*A*). This also afforded the opportunity to validate PARP1 L713F stabilization by an orthogonal readout and integrate cell cycle measurements in response to drug treatment, which could further inform on differential pharmacology. In total, the rescreen contained the annotated PARPi and 14 non-PARPi tested previously, as well as two additional PARPi reported to be PARP1-(MC2050) and PARP2-selective (MC3474; Compound 1), respectively (24). The compounds were tested at 10 μM and biosensor abundance was measured after 16 h. Hits were defined as having statistically significant ($p < 0.05$) abundance changes from the dimethyl sulfoxide (DMSO) (negative) control.

All PARPi significantly increased PARP1 L713F-GFP abundance, but only a few non-PARPi (PF-3758309, bisindolylmaleimide I, AZ960, Go 6983, and ACY-1083) also met this threshold, essentially mirroring the L713F-nLuc biosensor reported earlier (17). Notably, the DNA methyltransferase trappers, decitabine and azacitidine, did not meaningfully increase L713F-GFP, in contrast to the nLuc reporter. Almost all
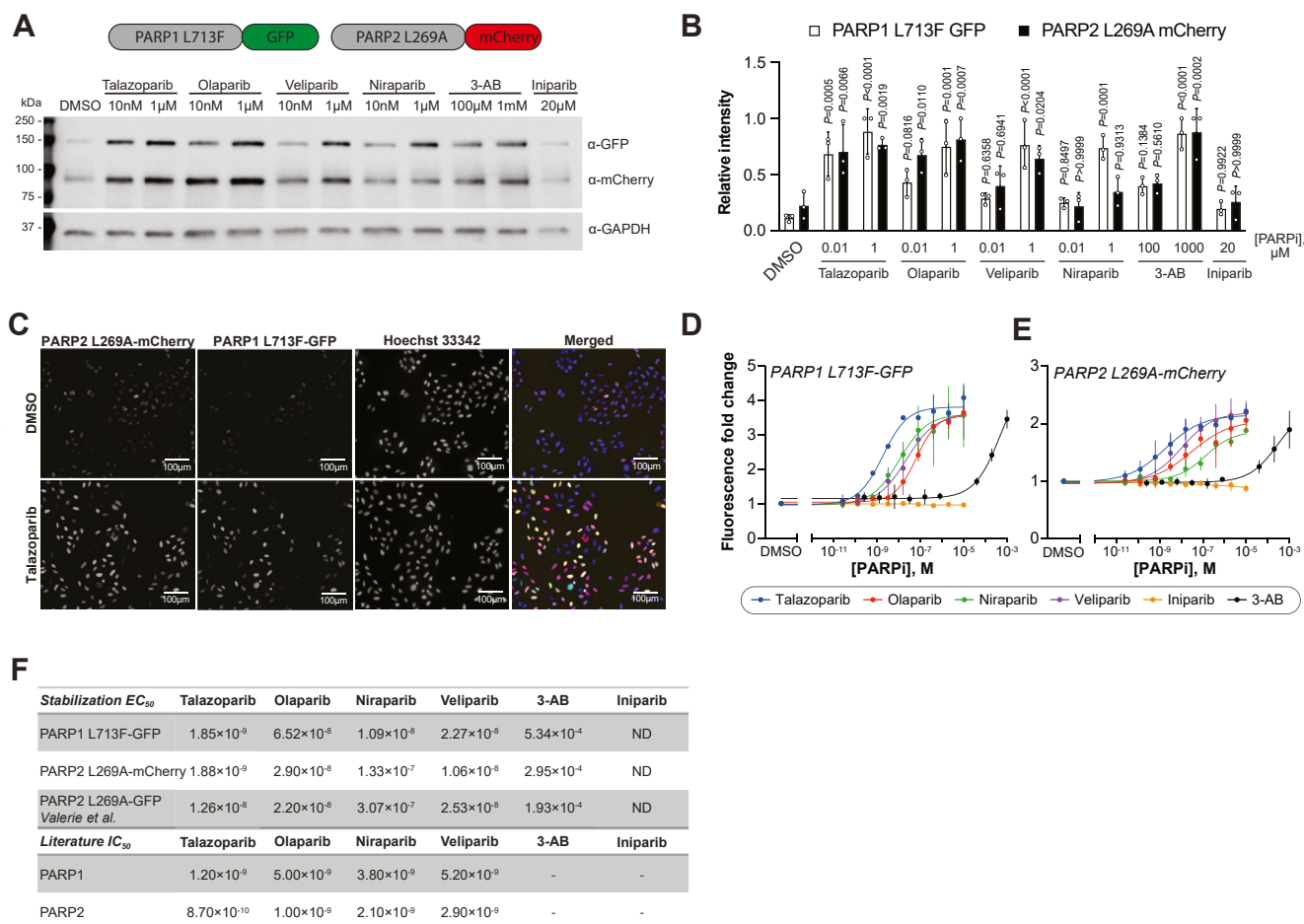
Figure 1. Establishment of a duplexed PARP1/2 CeTEAM drug biosensor platform. *A*, a representative Western blot of PARP1 L713F-GFP and PARP2 L269A-mCherry abundance after 24 h with PARP inhibitors (PARPi) at indicated concentrations. *B*, densitometric quantification of PARP1 L713F-GFP (*white*) and PARP2 L269A-mCherry (*black*) relative to GAPDH and normalized to the highest value observed for each reporter. Means ± SD from n = 3 independent experiments shown. Statistical significance was determined by one-way ANOVA with Dunnett's post test with comparison to the DMSO control (F[DFn, DFd]: 11.67 [11, 24]; $p < 0.0001$). *C*, representative live-cell fluorescence micrographs of L713F-GFP (*green*) and L269A-mCherry (*red*) biosensors after 24-h DMSO or 10 μM talazoparib. Cell nuclei identified by Hoechst staining (*blue*; merged image in color) and scale bars represents 100 μm. *D*, live-cell L713F-GFP fluorescence fold change following PARPi concentration gradients for 24 h and normalization to DMSO controls. Means ± SD from n = 3 experiments with lines-of-best-fit shown. *E*, live-cell L269A-mCherry fold change by fluorescence microscopy, as in D. Means ± SD (n = 3 experiments) with lines-of-best-fit shown. *F*, observed stabilization EC$_{50}$ values for PARP1 L713F-GFP and PARP2 L269A-mCherry with indicated PARPi compared to PARP2 L269A-GFP data from *Valerie et al.* (17). Reported biochemical IC$_{50}$ values are given for reference. ND, not determined. CeTEAM, cellular target engagement by accumulation of mutant; DMSO, dimethyl sulfoxide; PARP, poly (ADP-ribose) polymerase.

PARPi also significantly increased PARP2 L269A-mCherry abundance, except for MC2050 and MC3474 (Fig. 2C). AZD5305, a compound previously identified as a highly specific PARP1 inhibitor (25, 26), comparably stabilized PARP2 at this high concentration (Fig. 2, *B* and *C*). The same non-PARPi that increased L713F-GFP also affected PARP2 L269A-mCherry, except for the two protein kinase C inhibitors (PKCi; bisindolylmaleimide I and Go 6983), which, in contrast to PARP1 L713F, significantly decreased PARP2 L269A abundance. Another non-PARPi, AT9283, showed a modest but significant effect on PARP2 that was not seen with PARP1.

We then performed a cross-comparison of hits for PARP1 and PARP2 to help identify any clear trends (Fig. 2D). Of the compounds tested, 32 significantly stabilized both PARP1 and PARP2, while eight did not appreciably affect either. All nonresponsive molecules were annotated non-PARPi.

Therefore, apart from select molecules, effects on PARP2 L269A abundance generally aligned with PARP1 L713F at the 10 μM screening concentration.

Intracellular selectivity profiling of PARPi with CeTEAM

Initial follow-up of non-PARPi hits confirmed that the broad-spectrum protein kinase c inhibitors, bisindolylmaleimide I and Go 6983, selectively increased PARP1 L713F-GFP abundance in a concentration-responsive manner (Fig. S3, *A* and *B*). However, systematic dissection of these molecules revealed that both are autofluorescence artifacts at emission wavelengths ~600 nm (Fig. S4, *A*–*E*), in agreement with earlier reports using fluorescence-based detection systems (27).

In parallel with our analysis of non-PARPi, we conducted concentration gradient experiments with the expanded PARPi
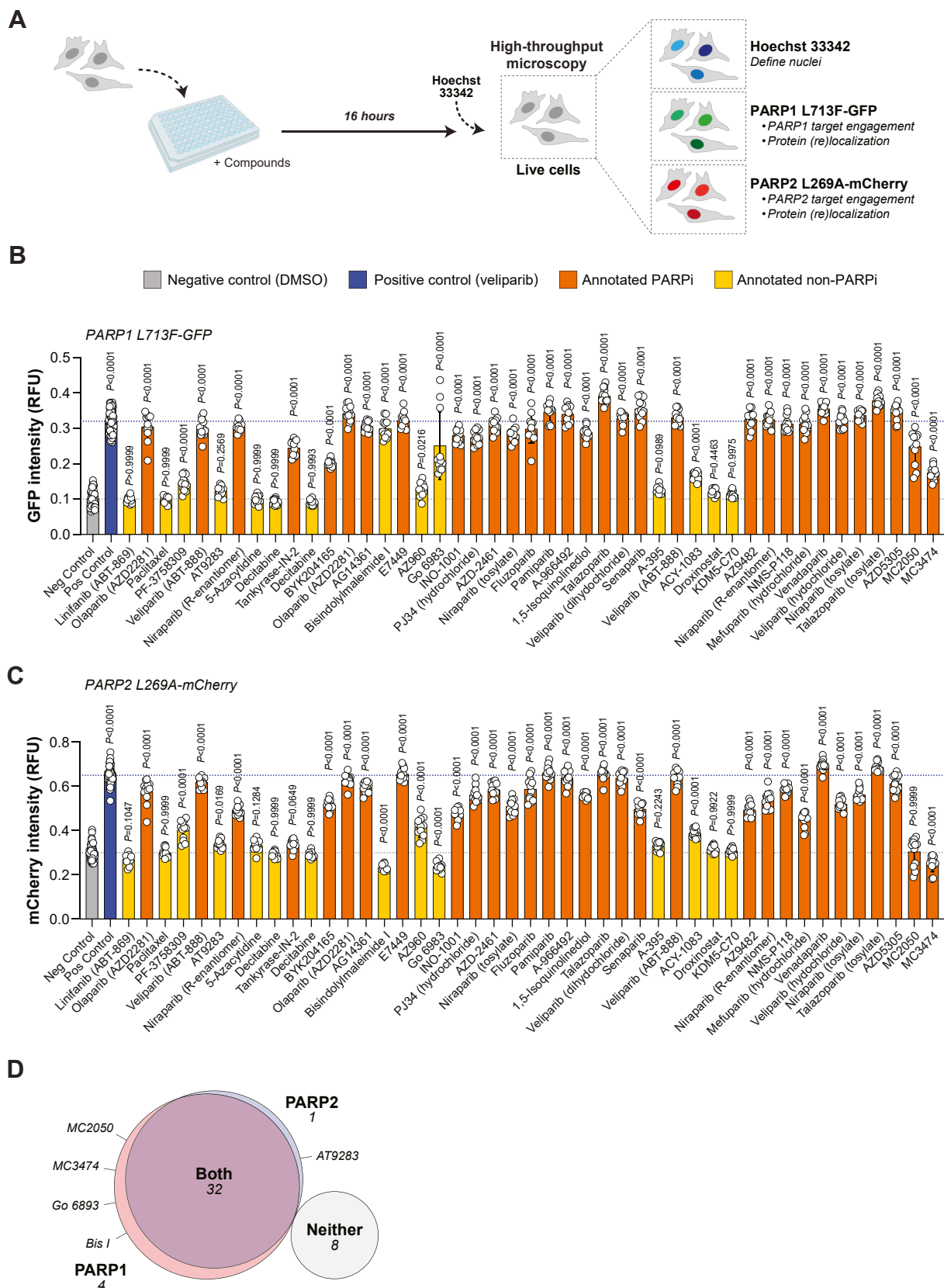
Figure 2. Rescreening of potential PARP1/2 biophysical modulators with duplexed PARPi biosensors. *A*, overview of rescreening procedure for PARP1 (GFP) and PARP2 (mCherry) target engagement by live-cell fluorescent microscopy. Nuclei are identified by Hoechst 33342 staining. *B*, PARP1 L713F-GFP intensity following 10 μM PARPi (*orange*, 31 total) and non-PARPi (*yellow*, 14 total). Negative (DMSO, *gray*) and positive controls (10 μM veliparib, *blue*) are shown with intensity reference lines. Means shown for three replicate wells (four images per well) ± SD. Statistical significance was determined by one-way ANOVA with Dunnett's post test with comparison to the DMSO control (F_{PARP1}[DFn, DFd]: 212.1 [46, 613], $p < 0.0001$; F_{PARP2}[DFn, DFd]: 274.9 [47, 630],

library using the duplexed PARP1/2 biosensors to establish a compendium of PARP1 and PARP2 binding in live cells (Fig. 3A). Comparative analysis of PARP1 L713F-GFP (Fig. 3B) and PARP2 L269A-mCherry (Fig. 3C) stabilization dynamics,

alongside literature-derived IC_{50} values, facilitated a robust evaluation of each inhibitor's cellular efficacy, as summarized in Table 1 and depicted in Figure S5. As before, talazoparib, olaparib, veliparib, and 3-AB were equipotent for PARP1 and
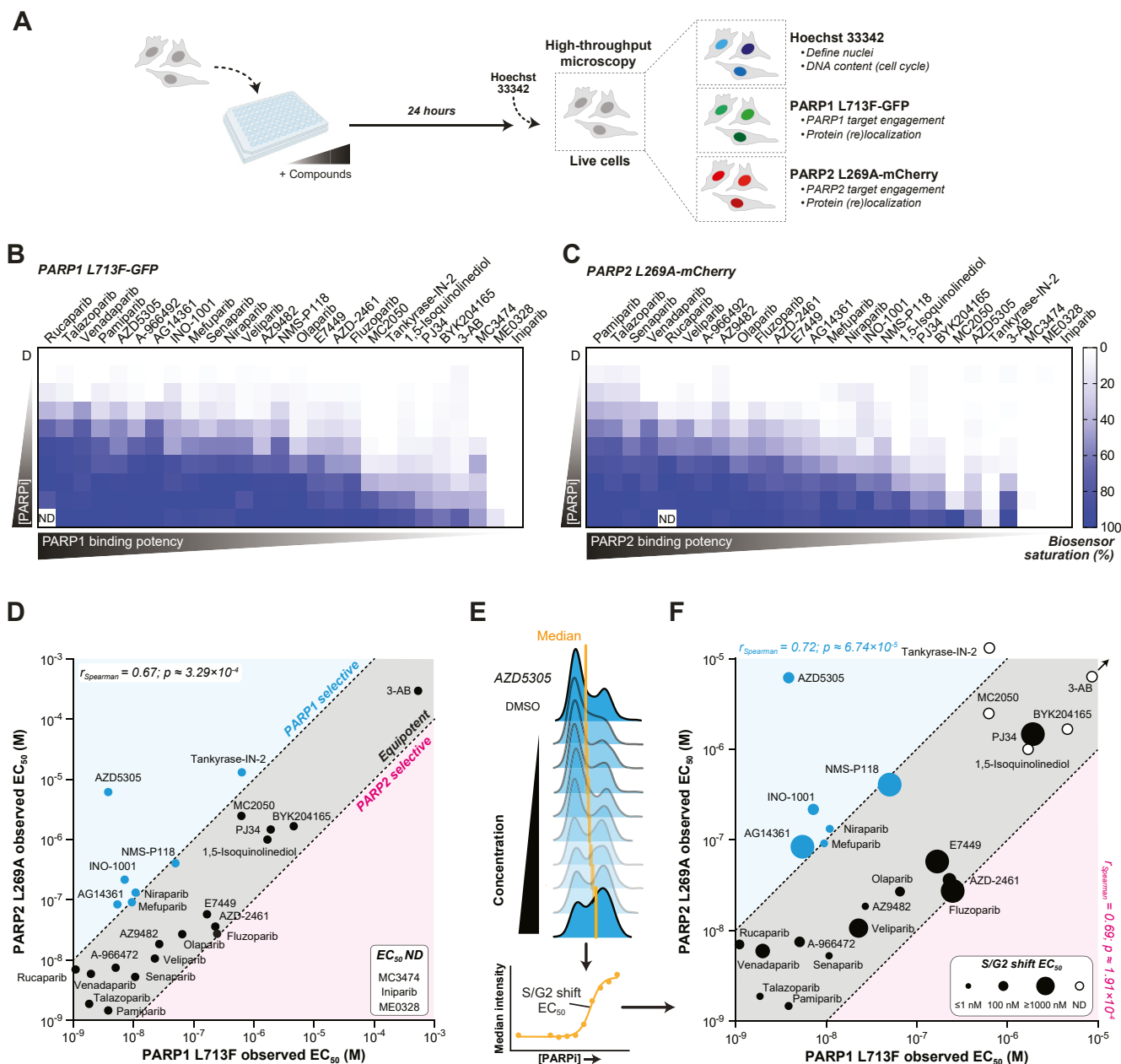

Figure 3. Intracellular PARP inhibitor selectivity and trapping profiling with CeTEAM. *A*, experimental procedure for concentration-dependent PARP1 L713F-GFP and PARP2 L269A-mCherry stabilization and cell cycle perturbations (Hoechst 33342) by PARPi with live-cell fluorescent microscopy. *B*, relative PARP1 L713F-GFP intensity expressed as fold change DMSO control after 24 h of a PARPi gradient. Means shown from n = 3 experiments. *C*, relative PARP2 L269A-mCherry intensity, as shown in B. *D*, two-dimensional comparison of PARPi stabilization EC_{50} values toward PARP1 L713F-GFP and PARP2 L269A-mCherry. *Blue* – ≥10-fold PARP1 selective; *red* – ≥10-fold PARP2 selective; *gray* – <10-fold selectivity (equipotent). Spearman correlation r = 0.67; $p \approx 3.29 \times 10^{-4}$. Values derived from n = 3 experiments from B and C. *E*, derivation of S/G2-phase shift EC_{50} from the median Hoechst intensity (DNA content). *F*, three-dimensional comparison of PARP1 (*x-axis*; *blue*) and PARP2 (*y-axis*; *red*) engagement EC_{50} values and PARP trapping EC_{50} values (*circle* size) for tested PARPi. Circle size – ≤1 nM (smallest) to ≥1000 nM (largest), or *open circle* – EC_{50} not determined (ND). A representative experiment from n = 3 is used for S/G2 shift EC_{50} overlay. Spearman correlation r = 0.72; $p \approx 6.74 \times 10^{-5}$ for PARP1. Spearman correlation r = 0.69; $p \approx 1.91 \times 10^{-4}$ for PARP2. CeTEAM, cellular target engagement by accumulation of mutant; DMSO, dimethyl sulfoxide; PARP, poly (ADP-ribose) polymerase.

$p < 0.0001$). *C*, PARP2 L269A-mCherry intensities for the rescreened compounds, as in B. *D*, Venn diagram representation of statistically significant hits for PARP1 and PARP2. Compounds affecting neither target are also shown, while those stabilizing solely one target are named. RFU, relative fluorescence units; DMSO, dimethyl sulfoxide; PARP, poly (ADP-ribose) polymerase.

Table 1
Comparison of CeTEAM stabilization EC_{50} values and reported biochemical IC_{50} values of tested PARPi toward PARP1/2 (M)

PARPi	PARP1 IC_{50}	PARP1 L713F-GFP EC_{50}	PARP2 IC_{50}	PARP2 L269A-mCherry EC_{50}
Talazoparib	1.20×10^{-9a}	1.854×10^{-9}	8.70×10^{-10a}	1.875×10^{-9}
Pamiparib	9.00×10^{-10a}	3.839×10^{-9}	5.00×10^{-10a}	1.467×10^{-9}
Niraparib	3.80×10^{-9a}	1.093×10^{-8}	2.10×10^{-9a}	1.325×10^{-7}
Veliparib	5.20×10^{-9a}	2.274×10^{-8}	2.90×10^{-9a}	1.062×10^{-8}
Rucaparib	1.40×10^{-9a}	1.110×10^{-9}	1.40×10^{-9a}	7.013×10^{-9}
A-966492	1.00×10^{-9b}	5.081×10^{-9}	1.50×10^{-9b}	1.201×10^{-8}
Olaparib	5.00×10^{-9a}	6.520×10^{-8}	1.00×10^{-9a}	2.689×10^{-8}
PJ34	1.10×10^{-7a}	1.913×10^{-6}	8.60×10^{-8a}	1.471×10^{-6}
Mefuparib	3.20×10^{-9a}	9.477×10^{-9}	1.90×10^{-9a}	9.156×10^{-8}
MC3474	2.04×10^{-6a}	ND	3.4×10^{-7a}	ND
MC2050	9.30×10^{-9a}	6.246×10^{-7}	5.49×10^{-7a}	2.496×10^{-6}
AZD5305	3.00×10^{-9a}	3.847×10^{-9}	1.40×10^{-6a}	6.172×10^{-6}
Tankyrase-IN-2	7.1×10^{-7a}	7.885×10^{-7}	-	1.315×10^{-5}
AZ9482	1.00×10^{-9b}	2.701×10^{-8}	1.00×10^{-9b}	1.849×10^{-8}
Senaparib	4.80×10^{-10a}	1.074×10^{-8}	1.60×10^{-9a}	5.257×10^{-9}
INO-1001	5.0×10^{-8b}	7.198×10^{-9}	-	2.172×10^{-7}
NMS-P118	9.00×10^{-9a}	5.016×10^{-8}	1.39×10^{-6a}	4.076×10^{-7}
Venadaparib	1.40×10^{-9a}	1.986×10^{-9}	1.00×10^{-9a}	5.935×10^{-9}
AG14361	1.40×10^{-8b}	5.458×10^{-9}	-	8.399×10^{-8}
E7449	2.00×10^{-9a}	1.679×10^{-7}	1.00×10^{-9a}	5.776×10^{-8}
AZD2461	5.00×10^{-9a}	2.294×10^{-7}	2.00×10^{-9a}	3.626×10^{-8}
Fluzoparib	1.46×10^{-9a}	2.49×10^{-7}	-	2.734×10^{-8}
BYK204165	7.35×10^{-9a}	4.607×10^{-6}	4.17×10^{-6a}	1.669×10^{-6}
1,5-Isoquinolinediol	$1.8–3.7 \times 10^{-7b}$	1.694×10^{-6}	-	1.001×10^{-6}
ME0328	6.30×10^{-6a}	ND	1.08×10^{-5a}	ND
3-AB	5.00×10^{-8b}	5.338×10^{-4}	-	2.953×10^{-4}
Iniparib	-	ND	-	ND

[a] Biochemical assay.
[b] Cell-based assay.
Abbreviations: ND, not determined.

PARP2, while iniparib was inactive, and niraparib was ~14-fold more potent toward PARP1.

Unsurprisingly, clinical-grade PARPi were typically the most potent for both PARPs (low nanomolar), while early generation PARPi (*e.g.*, PJ34, BYK204165, 1,5-isoquinolinediol, and 3-AB) or those not intended to directly target PARP1/2 (*e.g.*, Tankyrase-IN-2, ME0328) were significantly worse (Table 1). Tankyrase-IN-2 is reported to predominantly target TNKS1/2 but has low level activity toward PARP1 (28), while ME0328 preferentially targets PARP3 (29). Furthermore, the next generation PARPi, senaparib (IMP4297), and venadaparib, equipotently engaged PARP1/2 biosensors in the low nanomolar range like other potent PARPi, such as A-966492 and rucaparib (Table 1), in line with biochemical inhibition data toward PARP1 and PARP2 (senaparib: 0.48 and 1.6 nM, venadaparib: 0.8 and 3.0 nM, respectively) (30, 31).

Some PARPi also bound PARP1 and PARP2 much worse than anticipated. For example, PJ34 was >10-fold worse toward both PARPs in our assay as compared to reported IC_{50} values (Fig. 3D and Table 1). Additionally, despite published specificity for PARP2 (24), MC3474 was one of the least potent PARPi in our assay, which may relate to its relatively high biochemical IC_{50} values (Fig. S5 and Table 1). These demonstrated a similar phenomenon to other early PARPi (*e.g.*, 3-AB), where intracellular potency is significantly compromised, and may relate to cellular permeability and efflux.

Most of the expanded PARPi library was essentially equipotent binders of both PARPs, but some appeared to demonstrate slight selectivity toward PARP1 or PARP2. To facilitate comparisons of PARPi selectivity, we performed a pairwise analysis of PARP1 and PARP2 biosensor saturation

for each PARPi and compared their apparent EC_{50} values (Fig. 3D). We arbitrarily defined selectivity as > ~10-fold differential potency (cyan or magenta regions) and equipotency as <10-fold preference (gray region) for either PARP. As expected, most inhibitors fell within the equipotency designation, as supported by PARP1 and PARP2 biosensor binding potencies being highly correlative ($r_{Spearman}$ = 0.67, $p \approx 0.000329$).

While some inhibitors had negligible selectivity toward PARP1 (*e.g.*, rucaparib and MC2050), AZD5305, INO-1001, niraparib, AG14361, mefuparib, NMS-P118, and tankyrase-IN-2 definitively favored PARP1 binding, although tankyrase-IN-2 was significantly less potent overall. At 10 µM, we initially saw that AZD5305 exhibited comparable stabilization of both biosensors (Fig. 2, B and C). However, it displayed markedly higher specificity toward PARP1 over PARP2 over an extended concentration range, as evidenced by a marked difference in stabilization EC_{50} values—3.9 nM *versus* 6.2 µM, respectively (~1600-fold; Table 1, Fig. 3D). Our measures of apparent PARP1/2 binding for AZD5305 align well with reported biochemical and intracellular IC_{50} values (25, 26). We could also confirm the slight specificity of MC2050 for PARP1 in our cellular assays (PARP1: 625 nM, PARP2: 2482 nM; (24)), albeit with significantly worse efficacy than AZD5305 despite their similar biochemical potencies. Prior to the disclosure of AZD5305, NMS-P118 was reported as one of the first selective PARP1i (~150-fold over PARP2, (32)). However, our results reflected a much smaller selectivity window in cells (~10-fold; 50.2 and 408 nM, respectively). Interestingly, the early generation PARPi, INO-1001, was quite robust in our assay and yielded a surprising ~30-fold preference for PARP1

over PARP2 (apparent PARP1 EC_{50}: ~7.9 nM, PARP2 EC_{50}: ~217.2 nM), although we did not find reports with conclusive data describing its PARP1/2 inhibitory potency.

While PARP1-selective molecules have been disclosed, there are no validated PARP2-selective inhibitors, to the best of our knowledge. In our assay, AZD2461 and fluzoparib demonstrated slight, but insignificant, selectivity for PARP2 (~6- and 9-fold, respectively; Table 1, Fig. 3D). Of the remaining molecules, none demonstrated appreciable preference for PARP2 binding.

In addition to live-cell fluorescence microscopy, we validated these findings for many PARPi by Western blot analysis —confirming that detected fluorescence changes were proportional to protein abundance changes (Fig. S6, A and B). Collectively, these results suggest that a duplexed PARP1/2 CeTEAM platform can effectively profile PARPi selectivity in a scalable assay with live, single cells.

Trapping-like cell cycle shifts strongly correlate with PARP1/2 binding potency

Related to the synthetic lethal DNA damage elicited in homologous recombination-defective cancer cells, many clinical PARPi can trap PARP1 and PARP2 on DNA as part of their anticancer mechanism of action (1, 33). Previously, we and others have shown that measuring DNA content (cell cycle) is a suitable proxy readout of the DNA replication stress/S-phase delay and subsequent G2 arrest resulting from PARP trapping (17, 34). There, we defined trapping phenotypes as PARPi that both engaged the PARP1 biosensor and elicited an S/G2 shift in the cell cycle. While this approach provides valuable insights at scale, we acknowledge its limitations in directly assessing PARP retention on DNA, which may be most relevant for PARPi without reported trapping activity.

To profile how this expanded library of PARPi influenced cell cycle dynamics in relation to PARP1 and PARP2 binding, our experiments in PARP1/2 biosensor cells were complemented with the cell permeable DNA stain, Hoechst 33342 (Figs. 3A, S7). As before (17), this method enabled us to measure increases in trapping-like S/G2-phase character, reported as EC_{50} value shifts in median Hoechst intensity, which further permitted ranking on these parameters (Fig. 3E, Table 2). Juxtaposition of these data with PARP1/2 biosensor binding can give insights to potential on-*versus* off-target activity of PARPi.

Our scaled approach also afforded the possibility of gauging the quality of PARP trapping-like phenotypes based on concentration-dependent cell cycle dynamics (Fig. S7). Visual inspection of the cell cycle distributions revealed that S/G2-enriched profiles do not manifest uniformly. For example, talazoparib, a potent PARP1/2 trapper, exhibited an initial increase in S/G2-phase cells at low concentrations but transitioned to primarily an S-phase delay at higher concentrations. This is consistent with a tolerable level of trapping-related DNA damage at low concentrations that permits continuation through S-phase and then triggers the G2-phase DNA damage checkpoint, while at higher concentrations, the

Table 2
S/G2 shift EC_{50} values of tested PARPi from median Hoechst intensity changes

PARPi	S/G2 shift EC_{50} (M)
Talazoparib	2.78e-010
Pamiparib	2.96e-009
Niraparib	2.85e-009
Veliparib	5.28e-007
Rucaparib	2.37e-008
A-966492	4.16e-008
Olaparib	2.57e-008
PJ34	3.75e-006
Mefuparib	2.36e-009
MC3474	ND
MC2050	ND
AZD5305	6.07e-008
Tankyrase-IN-2	ND
AZ9482	3.51e-010
Senaparib	3.98e-010
INO-1001	5.97e-008
NMS-P118	5.88e-006
Venadaparib	1.97e-007
AG14361	1.12e-006
E7449	3.97e-006
AZD2461	1.46e-007
Fluzoparib	4.63e-005
BYK204165	ND
1,5-Isoquinolinediol	ND
ME0328	ND
3-AB	ND
Iniparib	ND

Abbreviations: ND, not determined.

extent of DNA replication-associated damage prohibits completion of S-phase. Senaparib also demonstrated such a profile, in support of it being a potent PARP1/2 binder and trapper. On the other hand, PARPi with more modest S/G2 shifts, such as venadaparib or AZD5305, induce G2-phase accumulation but fail to progress to predominantly S-phase arrest at higher concentrations, perhaps due to less efficient PARP retention by these inhibitors.

We then combined the median Hoechst intensity changes (S/G2 shift EC_{50} values) with the PARP1 L713F-GFP and PARP2 L269A-mCherry to give insights on how these phenotypes may be influenced by PARP1 and/or PARP2 binding. Overall, inhibitors that were the most potent binders of both PARP1 and PARP2 generally yielded the most potent S/G2 shifts, whereas the less potent binders were generally poor (Fig. 3F, Table 2). Both PARP1 and PARP2 biosensor binding potency highly correlated with the degree of S/G2-phase enrichment ($r_{Spearman}$ = 0.72 [$p \approx 0.0000674$] and 0.69 [$p \approx 0.000191$], respectively). Among these, the next generation PARPi, senaparib, was among the most potent (0.40 nM EC_{50}), along with talazoparib and AZ9482 (0.28 and 0.35 nM, respectively). There were some exceptions to this trend. Veliparib was a potent binder to both PARP1 and PARP2 but had a significantly worse effect on S/G2 enrichment (528 nM EC_{50}), in line with previous data (17, 32). Similarly, venadaparib potently engaged both PARP1 and PARP2 in our assay (1.99 and 5.94 nM, respectively) but had a corresponding S/G2 EC_{50} value of 197 nM. The PARP1-selective inhibitor, AZD5305 also demonstrated a robust trapping-like phenotype but was comparatively inferior to other potent, dual PARP1/2 inhibitors, such as senaparib (60.7 nM *versus* 0.4 nM S/G2 EC_{50}, respectively). On the other hand, PJ34, tankyrase-IN-2,

and 3-AB, which were among the worst PARP1/2 binders, had minimal (PJ34–3.75 μM EC$_{50}$) or no observable activity (tankyrase-IN-2, 3-AB). Thus, our observations align with the prevailing view that PARP trapping is predominantly driven by inhibitory potency but can also be strongly influenced by allosteric effects.

Differential PARP1/2 selectivity trends between two primary PARPi pharmacophores

Apart from a handful of reported PARPi, most clinical drugs equipotently inhibit PARP1/2 activity (4), but enzymatic IC$_{50}$ values may not necessarily align with biophysical measures of binding. Insights from biophysical readouts can inform on how well a compound binds to the target (35), which may be even more informative in a physiologically relevant, intracellular environment. From the literature, we note that niraparib is reported to inhibit PARP1 and PARP2 activity equipotently (3.8 and 2.1 nM, respectively (36)); however, biophysical measures have indicated that niraparib binds ∼50-fold worse to PARP2 (26).

We noticed similar biophysical trends for other benzimidazole carboxamide derivatives, specifically those with similar structures to niraparib (rucaparib, veliparib, and NMS-P118), while other structural classes of PARPi (olaparib and talazoparib) more closely resembled the equipotency of enzymatic assays. We then revisited our PARP1/2 biosensor binding data and saw that the PARPi with slight PARP1 selectivity were enriched for these same inhibitor subtypes—namely AG14361, mefuparib, niraparib, and NMS-P118 (Fig. 3D). Likewise, the molecules with modest PARP2 selectivity appeared to be enriched with phthalazinone derivatives similar to olaparib. These insights suggested that PARP1 and PARP2 selectivity may already be engrained in prevailing PARPi pharmacophores.

To investigate these observations more systematically, we employed the chemoinformatics server from ChemMine Tools to perform binned clustering and multidimensional scaling (2D MDS) on the PARPi library (37). These algorithms consider atom-by-atom similarities among all compound pairs using the Tanimoto coefficient, and, in the case of MDS profiling, translates this information to coordinates on a scatter plot. To account for the relatively small library of molecules we are comparing, we employed a Tanimoto coefficient cutoff of 0.4 for determining clustering hierarchies, which might otherwise be considered too lenient for analyzing larger, more diverse datasets. The resultant MDS plot reinforced several trends seen within the tested PARPi structures (Fig. S8). More condensed structures, such as 3-AB, 1,5-isoquinolinediol, and veliparib, were clustered in one quadrant, while elongated structures, such as MC3474, MC2050, and AZD5305, were enriched in another quadrant. Of note, the two reported PARP1-selective inhibitors, AZD5305 and NMS-P118, clustered together, suggesting their structures are highly similar.

Our chosen similarity cutoff generated 16 similarity clusters, which successfully identified two major groupings: benzimidazole carboxamide derivatives (niraparib-like, cluster 4) and olaparib-like phthalazinone derivatives (cluster 6; Fig. S8). NMS-P118, veliparib, and INO-1001 were clustered adjacent to niraparib derivatives, while AZD5305 was in between the two large clusters—indicating that its structure contains elements from both subgroups. To understand the relationship between structural similarity and binding selectivity, we then overlaid the clustering data onto our two-dimensional analysis of PARP1 and PARP2 binding (Fig. 4). This visualization demonstrated a clear segregation of PARPi selectivity based on their inherent chemical structures. Earlier generation PARPi with smaller pharmacophores were generally the least potent binders of PARP1 and PARP2 (clusters 9–15). More importantly, there was a clear deviation between niraparib-like molecules and those related to olaparib. The former, which included closely related INO-1001 and NMS-P118, generally had >10-fold preference for PARP1, while the latter trended toward PARP2 selectivity and was punctuated with AZD-2461 and fluzoparib being the most PARP2-selective. Likewise, AZD5305, which bears similarity to both series, is uniquely selective for PARP1. Overall, the results strongly suggest that the two prominent series of PARPi have inherent binding biases, which may be starting points for the next generation of highly selective drugs.

HPF1 depletion modestly affects PARPi binding potency but additively promotes trapping-like cell cycle changes

HPF1 is known for its essential role in regulating PARP activity *via* redirection of PARylation activity toward histone serine residues in response to DNA damage (13). As part of this mechanism, HPF1 contributes a key glutamine residue (Glu284) to the PARP1 and PARP2 active sites that facilitates rapid PAR initiation (12, 38). Despite its low cellular abundance relative to PARP1, HPF1 effectively influences PAR synthesis by a "hit-and-run", catalytic-like mechanism (38). Earlier *in vitro* studies have suggested that the presence of HPF1 slightly improves affinity of PARPi for PARP1 but not PARP2 (15); however, its impact on PARPi binding in cells has not been comprehensively studied.

To determine how HPF1 influences PARPi binding to PARP1/2, we complemented the duplexed PARP1/2 CeTEAM biosensor cells with doxycycline-regulable shRNA toward HPF1 (Fig. 5). First, we generated three shRNAs targeting HPF1 and validated their knockdown efficiency at both the mRNA level by reverse transcription quantitative PCR (each >∼90%) and protein level by Western blot analysis (each >∼80%), demonstrating significant reductions in HPF1 expression (Fig. 5, A−C). We then selected one hairpin (shHPF1 #1) for functional characterization.

Next, we assessed how HPF1 knockdown affected the binding dynamics of talazoparib, olaparib, niraparib, veliparib, 3-AB, and iniparib (Fig. 5, D−G). PARPi binding curves for a control hairpin (shNT) were similar to earlier profiles (Fig. 1, E and F). As expected, both biosensors were unaffected by iniparib irrespective of HPF1 levels. Like data with purified proteins, HPF1 had subtle effects on observed binding of other
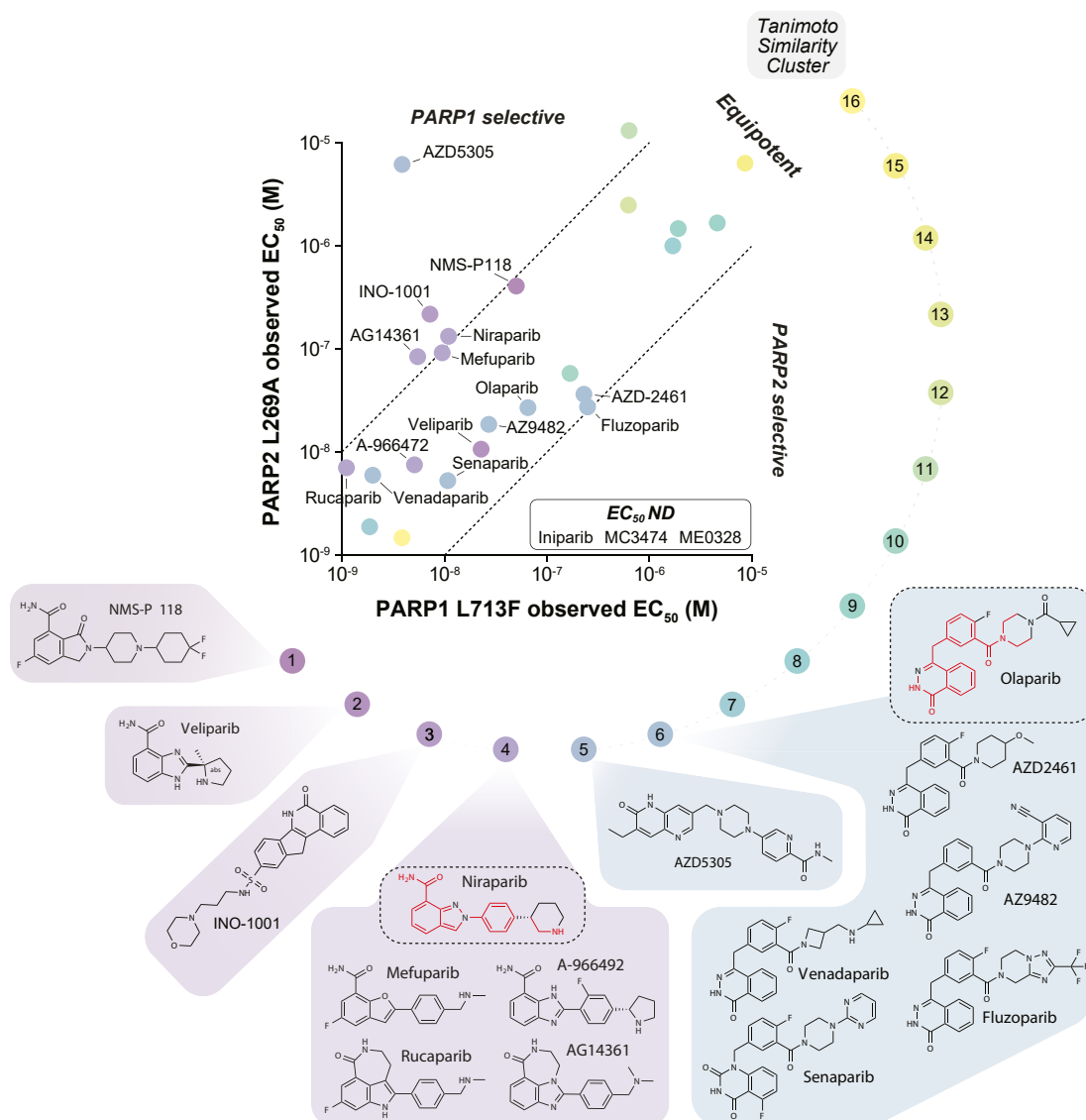
Figure 4. PARPi structural similarity profiling reveals pharmacophores with inherent PARP1/2 binding selectivity. Structural similarity clustering was performed with ChemMine Tools (Tanimoto coefficient cutoff of 0.4) and overlaid onto the two-dimensional PARP1 L713F-GFP and PARP2 L269A-mCherry data (from Fig. 3D). Similarity clusters (number 1–16) in color scale and PARPi structures from clusters with divergent selectivity profiles are shown. Highly similar moieties from niraparib and olaparib that are shared within relevant clusters are highlighted in *red*.

PARPi to PARP1 and PARP2. Observed stabilization of the PARP1 biosensor was generally unchanged with clinical grade inhibitors while PARP2 binding was generally enhanced by ∼2-3-fold following HPF1 depletion (Fig. 5G and Table 3). Notably, talazoparib binding was improved by ∼2-fold by HPF1 depletion for both PARP1 and PARP2. Thus, HPF1 can influence PARPi binding to PARP1 and PARP2 in cells, which has important implications for intracellular PARPi selectivity. Additionally, our data demonstrate that genetic components can be layered onto CeTEAM-based assays to investigate the contribution of other proteins to observed binding potencies of a given target.

In addition to assessing differences in target engagement following HPF1 knockdown, we sought to evaluate its impact on trapping-like cell cycle changes. As HPF1 binds PARP1/2 following helical domain (HD) destabilization (12), HPF1 depletion should theoretically increase PARP trapping on DNA

by disrupting serine PARylation of histones and further sensitize cells to trapping PARPi (16, 39). Indeed, as seen previously (16, 39), HPF1 depletion induced an S/G2-phase delay consistent with PARP trapping-related replication stress (Fig. 5, *H–J* and Table 4). The S/G2-phase shift induced by HPF1 depletion appeared to additively compound the effects of all tested trapping PARPi, whereas profiles for iniparib and 3-AB only exhibited the basal increase from HPF1 knockdown (Figs. 5, *H–J* and S9). Overall, the data suggest that HPF1 knockdown has an additive effect on PARPi-induced trapping—presumably by already retaining a fraction of the PARP pool onto DNA.

Discussion

PARPs are crucial players in cellular DNA repair and attractive drug targets. However, PARP1 and PARP2 have highly homologous catalytic domains, so truly selective PARPi
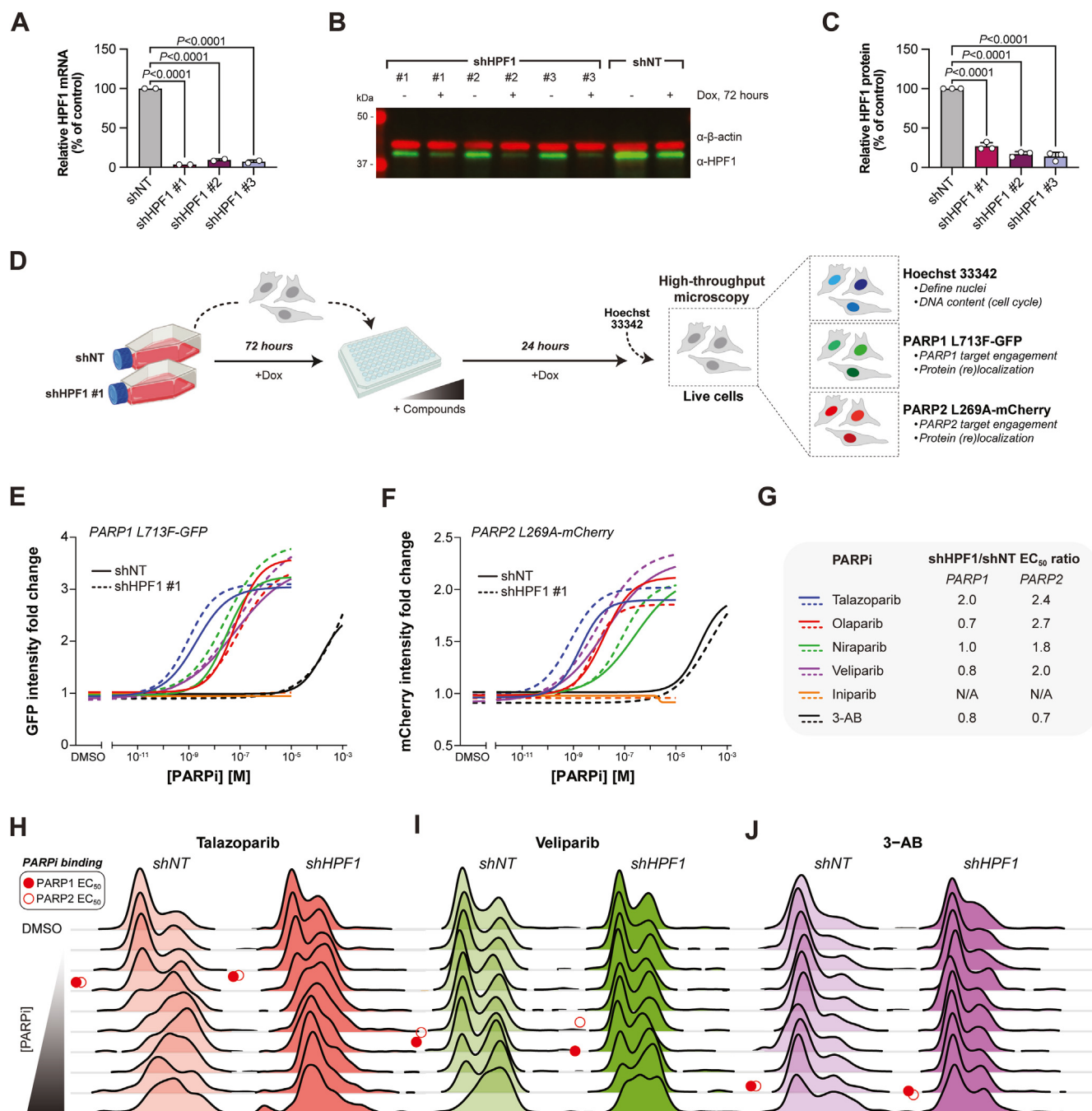
Figure 5. An integrated CeTEAM-genetics approach to assess the influence of HPF1 on intracellular PARPi binding and S/G2 cell cycle shifts. *A*, RT-qPCR analysis of gene silencing efficiency by doxycycline-regulable shRNAs targeting *HPF1* (shHPF1 #1, shHPF1 #2, or shHPF1 #3) compared to nontargeting control (shNT). Gene expression levels were normalized to *β-actin* and expressed as percentage of shNT control. Means ± range from n = 2 biological replicates (three technical replicates for each). Statistics were determined by one-way ANOVA with Dunnett's post test and comparison to the shNT control (F[DFn, DFd]: 2370 [3, 4], *p* < 0.0001). *B*, representative HPF1 protein (*green*) knockdown after 72 h doxycycline by Western blot (from n = 3 experiments). β-actin (*red*) is used a loading control. *C*, quantification of HPF1 protein levels 72 h post knockdown (related to B). Means ± SD from n = 3 experiments (individual experimental values shown). Statistics were determined by one-way ANOVA and Dunnett's post test and comparison to shNT control (F[DFn, DFd]: 325.2 [3, 8], *p* < 0.0001). *D*, experimental set-up for live-cell PARP1 (GFP) and PARP2 (mCherry) target engagement and PARPi-induced S/G2 cell cycle shifts (Hoechst) by fluorescent microscopy following HPF1 knockdown. *E*, PARP1 L713F-GFP fluorescence intensity fold change in control (*solid line*) or HPF1 knockdown (*dashed line*) cells after talazoparib (*blue*), olaparib (*red*), niraparib (*green*), veliparib (*purple*), iniparib (*orange*), or 3-AB (*black*) gradients for 24 h. Data normalized to DMSO control. Lines-of-best-fit from n = 3 experiments. *F*, PARP2 L269A-mCherry fluorescence intensity fold change, as in E. *G*, shHPF1/shNT EC$_{50}$ value ratios (fold change) of talazoparib, olaparib, niraparib, veliparib, iniparib, and 3-AB stabilization toward PARP1 (L713F-GFP) or PARP2 (L269A-mCherry). N/A, not applicable *H*, representative cell cycle dynamics of control (shNT) or shHPF1 #1 cells after a talazoparib, veliparib (*I*), or 3-AB gradient (*J*) for 24 h, represented as a Ridgeline plot (related to *E and F*). *Red circles*–approximate stabilization EC$_{50}$ values for PARP1 (*closed*) or PARP2 (*open*) biosensors. CeTEAM, cellular target engagement by accumulation of mutant; HPF1, histone PARylation factor 1; 3-AB, 3-aminobenzamide; RT-qPCR, Reverse transcription quantitative PCR; DMSO, dimethyl sulfoxide.

Table 3
Comparison of PARPi EC$_{50}$ values in shNT or shHPF1 cells

PARPi	shNT (nM)	shHPF1 (nM)	logEC$_{50}$ p value[a]	shHPF1/shNT EC$_{50}$ ratio
PARP1 L713F-GFP EC$_{50}$				
Talazoparib	1.949	0.963	0.0209	2.0
Olaparib	63.80	30.96	0.4754	0.7
Niraparib	28.49	27.60	0.9528	1.0
Veliparib	63.47	81.47	0.7858	0.8
Iniparib	NA	NA	NA	NA
3-AB	147,300	187,000	0.3837	0.8
PARP2 L269A-mCherry EC$_{50}$				
Talazoparib	1.819	0.7461	0.0180	2.4
Olaparib	16.01	5.993	0.0155	2.7
Niraparib	140.2	78.68	0.6835	1.8
Veliparib	18.63	9.159	0.3355	2.0
Iniparib	NA	NA	NA	NA
3-AB	145,100	206,900	0.6325	0.7

[a] Two-tailed, unpaired t test; others are not significant.

have historically been difficult to identify. Traditional selectivity profiling is done with purified proteins, but this approach is highly dependent on the experimental conditions and omits several factors that can influence ligand binding, such as post-translational modifications, biomolecular interaction partners, cell permeability and efflux of the compound, and general space constraints within the intracellular environment. Thus, cell-based selectivity assays can afford novel insights to drug interactomes and overcome some limitations of biochemical approaches (11). Here, we evaluated PARPi binding to PARP1 and PARP2 using a multiplexed CeTEAM approach to generate live-cell selectivity and pharmacology profiles.

Overall, we found most PARPi are roughly equipotent binders of both PARP1 and PARP2 in cells with similar potency to *in vitro* measures. Among these were the next generation PARPi, senaparib, which has recently shown efficacy as a first-line option for advanced ovarian cancer (30, 40). Despite its promise in the clinic, relatively little is known about its potency and selectivity. Our results indicate robust binding to both PARP1 and PARP2 (10.7 and 5.3 nM, respectively)—similar to other potent, clinical-grade PARPi—thereby supporting its clinical activity. For PARPi that were significantly less potent in cells, it is conceivable that permeability and efflux conditions affected observed binding potency by limiting drug availability.

There were also PARPi with divergent selectivity (arbitrary selectivity ratio >10-fold), but primarily toward PARP1—including niraparib, INO-1001, AG14361, mefuparib, NMS-P118, tankyrase-IN-2, and AZD5305. Structural similarity analysis indicated that all these molecules, except for tankyrase-IN-2, contain similar elements imparting preference

for PARP1 binding. Most of these are extended benzimidazole carboxamide derivatives, like niraparib, or possess similarly elongated moieties, suggesting that this characteristic feature may be critical to disfavor binding to PARP2. Indeed, it has been reported that niraparib can sterically clash with the N terminus of αF in the PARP2 HD, which angles slightly differently from αF in PARP1 (23), so it would not be far-fetched to assume that similar steric interactions also affect similar molecules, leading to preferred PARP1 binding.

Notably, we did not find clear PARP2-selective inhibitors among the tested PARPi, although phthalazinone pharmacophores related to olaparib showed slight, but consistent, preferences for PARP2 over PARP1. Like the PARP1-selective molecules, PARP2-preferred binding may be driven by divergent interactions with αF in PARP1 and PARP2, as the orientations and amino acid compositions of these respective helices are slightly different. Indeed, a report on a selective PARP2 inhibitor not included in our study (IC$_{50}$: 12 nM, ∼40-fold over PARP1) suggested that steric clashing with Glu763 in PARP1 αF was responsible for observed selectivity (41). Interestingly, this compound is an olaparib derivative with high similarity to fluzoparib, the most PARP2-selective inhibitor we tested in our study. Bearing in mind these differences, as well as the influence of another cryptic helix adjacent to αF in PARP2 (42), are likely key to selective PARPi development in the future.

The discrepancies in selectivity for several PARPi were unexpected given the abundance of *in vitro* inhibition data supporting their equipotency. However, accurate measures of PARP1 and PARP2 inhibition can be difficult to attain due to their ability to automodify themselves, resulting in a tight

Table 4
Comparison of shNT and shHPF1 S/G2 shift EC$_{50}$ values by PARPi

PARPi	shNT (nM)	shHPF1 (nM)	logEC$_{50}$ p value[a]	shHPF1/shNT EC$_{50}$ ratio
Talazoparib	0.29	0.09	0.1001	3.2
Olaparib	14.4	1.89	0.1382	7.6
Niraparib	7.85	1.74	0.1295	4.5
Veliparib	709.1	55.0	0.0745	12.9
Iniparib	NA	NA	NA	NA
3-AB	NA	NA	NA	NA

[a] Two-tailed, unpaired t test; others are not significant.

ASBMB

J. Biol. Chem. (2025) 301(4) 108361 **11**

binding limit problem (which likely underestimates the actual potency of the inhibitor, (5)). On the other hand, measures of PARPi binding by fluorescence polarization have indicated that many niraparib-like molecules are more PARP1 selective (26), suggesting that these molecules are more selective than originally thought. Our approach can sidestep this limitation and may more accurately reflect how well the drug binds to the target.

AZD5305 has been touted as one of the first truly PARP1-selective inhibitors to date (25, 26), and our datasets with live cell CeTEAM selectivity profiling confirm its high selectivity for PARP1 over PARP2 by a remarkable ~1600-fold (3.9 nM *versus* 6.2 μM, respectively). Of all inhibitors tested, it was the only one that had such a high selectivity, which was also consistent over time (Fig. S10). It was recently reported that AZD5305 can still allosterically trap PARP2 onto DNA at higher concentrations (>1 μM), suggesting that it binds PARP2 above 1 μM and could influence intracellular selectivity and toxicity profiles (23). Notably, we could also confirm significant binding to PARP2 at ≥ 1 μM AZD5305 by both CeTEAM and CETSA (Fig. S2). Indeed, binding and trapping of PARP2 has been implicated as the driver of hematological toxicities in patients treated with current PARPi (9, 10). However, based on our findings, there is a significant intracellular selectivity window (at least 1000-fold), implying that this can be largely avoided in a clinical setting. Thus, AZD5305 should be a promising molecule for selective PARP1 targeting and validates the use of a duplexed PARP1/2 CeTEAM assay to screen for novel, highly selective PARPi.

In addition to allosteric modulation of the HDs within PARP1 and PARP2, trapping is believed to be primarily driven by inhibitory potency—as inhibition also blocks PARP1/2 autoPARylation, thereby promoting their retention on DNA (5, 14, 43, 44). In agreement with this notion, we generally saw that PARP trapping phenotypes, as inferred from the degree of S/G2-phase shifts, correlate highly with binding potency, particularly when targeting PARP1/2 equipotently. Veliparib and, to a lesser extent, venadaparib were the clear exceptions to this trend, as they were the only potent PARPi that did not promote robust S/G2-phase cell cycle shifts. In the case of veliparib, this unique feature is likely driven by its considerably smaller size, which is unable to directly contact the HD, thereby promoting PARP release from DNA (23, 44). Interestingly, significant trapping-like phenotypes arise near the binding saturation point of the PARP1/2 biosensors, suggesting that veliparib's effect is primarily driven by inhibition. In agreement with earlier reports (25), we also see that AZD5305 promotes trapping-like phenotypes but to a lesser extent than most equipotent, clinical-grade PARPi (S/G2 shift EC_{50}: ~61 nM). This is conceivably due to a lack of extensive PARP2 trapping at lower drug concentrations, which occurs more readily with potent inhibitors equally targeting PARP1 and PARP2. Still, the effect of AZD5305 likely underscores the significant contribution of higher intracellular PARP1 abundance to overall PARP trapping phenotypes.

Another surprise was that the early generation PARPi, INO-1001 (Inotek/Genentech)—which was halted after Phase 1 clinical trials (45), was a potent PARP1/2 binder with impressive selectivity for PARP1 over PARP2 (~30-fold; 7.9 *versus* 217.2 nM, respectively). Notably, the INO-1001 selectivity profile was like that of niraparib, although insights to its PARP binding modality are unavailable for direct comparisons. Like AZD5305, INO-1001 also induced potent PARP trapping-like phenotypes (S/G2 shift EC_{50}: ~60 nM), but to a lesser extent than other clinical-grade inhibitors. Interestingly, concentration-limiting toxicities of INO-1001 were hematological, which may, in retrospect, relate to inhibition or trapping of PARP2. It is unclear why clinical development was ceased, as no serious adverse effects were reported from the clinical trials and pharmacokinetics data were promising, although concerns about liver toxicity may have played a role (46, 47). Nevertheless, our data suggest it might be worth considering INO-1001 as a tool for studies differentiating PARP1 and PARP2 biology.

Besides multiplexing drug biosensors, we added to the capabilities of CeTEAM by layering on a genetic perturbation element. Here, we sought to understand how HPF1, a critical component of the PARP1 and PARP2 catalytic sites, could influence binding of PARPi in cells. HPF1 was previously found to increase binding affinity of some PARPi for PARP1 but not PARP2 (5, 14). In our experiments with PARP1 L713F and PARP2 L269A, we instead saw generally improved PARPi binding when HPF1 was absent, particularly for PARP2. These discrepancies could be due to the nature of our PARP variants, as HPF1 preferentially binds PARP1/2 when the HD is in the open conformation and our mutants are constitutively flexible in the HD (6, 12, 48, 49). Indeed, HD deletion mutants of PARP1 have markedly higher affinity for HPF1 (16). Thus, HPF1 and ligand binding could have a compound effect on stability of these mutants. In line with this notion, we saw that knockdown of HPF1 induced a PARP trapping-like S/G2-phase shift, similar to cell cycle changes seen with known trapping inhibitors, indicating that HPF1 also affects PARP1/2 release from DNA. In support of this notion, HPF1 knockdown had an additive effect on S/G2-phase cell cycle shifts following addition of PARPi, again suggesting that both factors contribute to PARP1/2 retention.

In summary, we expand the capabilities of CeTEAM by both multiplexing PARP1 and PARP2 drug biosensors, while also incorporating knockdown of HPF1 to discern effects on PARPi binding and trapping-associated phenotypes. The expansion into multiplexed CeTEAM biosensors opens the door for higher throughput intracellular selectivity profiling assays, yielding potentially more accurate selectivity data overall. Meanwhile, the integration of genetic perturbation capabilities into CeTEAM platforms can facilitate the discovery of novel regulators of drug-target interactions and expand the scope of drug interactomes. In the context of PARP inhibitor development, our duplexed PARP1/2 CeTEAM platform should be a useful tool to aid the discovery of next generation, PARP1- or PARP2-selective inhibitors.

Experimental procedures

Cell lines and culturing conditions

U-2 OS osteosarcoma cells, HEK293T embryonic kidney epithelial cells, and CCRF-CEM human T lymphoblasts, were obtained from the American Type Culture Collection. U-2 OS and HEK293T cells were cultured in Dulbecco's modified Eagle's medium (DMEM) high glucose GlutaMAX medium (Thermo Fisher Scientific) supplemented with 1% Penicillin-Streptomycin (Thermo Fisher Scientific) and 10% fetal bovine serum (FBS; Thermo Fisher Scientific), while CCRF-CEM cells were cultured in RPMI 1640 Medium, GlutaMAX Supplement (Thermo Fisher Scientific) supplemented with 1% Penicillin-Streptomycin (Thermo Fisher Scientific) and 10% FBS. For *in vitro* fluorescent microscopy read-outs, DMEM, high glucose, no glutamine, no phenol red media (Thermo Fisher Scientific) supplemented with 1x GlutaMAX, 1% Penicillin-Streptomycin (Thermo Fisher Scientific) and 10% FBS (Thermo Fisher Scientific) was used. Cell cultures were maintained at 37 °C with 5% CO_2 in a humidified incubator. No additional authentication of cell lines was performed, and cell cultures were free from *mycoplasma* contamination but routinely screened (MycoAlert; Lonza).

Antibodies and chemicals

Anti-mCherry (rabbit polyclonal, cat. No. PA5-34974), donkey anti-rabbit Alexa Fluor 568 (cat. No. A10042) and goat anti-rabbit Alexa Fluor 488 (cat. No. A11008) were obtained from Thermo Fisher Scientific, anti-PARP2 (rabbit polyclonal, cat. No. 55149-1-AP) and anti-PARP1 recombinant antibody (rabbit recombinant, cat. No 80174-1-RR-20) were acquired from Proteintech, anti-GAPDH (rabbit polyclonal, cat. No. ab9485) and anti-NUDT5 (rabbit monoclonal, cat No. ab129163) was purchased by Abcam, anti-β-actin (mouse monoclonal, A5441) was obtained from Sigma-Aldrich, anti-HPF1 (rabbit monoclonal, 90876), was acquired from Cell Signaling Technology, anti-PARP1 (mouse monoclonal, sc8007), anti-GFP (mouse monoclonal, sc-9996). and anti-SOD1 (mouse monoclonal, cat No. sc-17767) were purchased from Santa Cruz Biotechnology. Doxycycline hydrochloride (Sigma-Aldrich) was dissolved in MilliQ water (2 mg/ml) and used at 0.75 µg/ml. Talazoparib, niraparib, olaparib, veliparib, AZ9482, senaparib, tankyrase-IN2, and INO-1001 (MedChemExpress) were dissolved in DMSO to a stock of 10 mM. Iniparib (MedChemExpress) was dissolved in DMSO to a stock of 20 mM. 3-aminobenzamide (3-AB; Sigma-Aldrich) was dissolved in DMSO to a stock of 100 mM. A-966492, pamiparib, PJ34, MC2050, MC3474, mefuparib, AZD5305, and rucaparib were kindly provided by the Rotili Lab and dissolved in DMSO at 10 mM. NMS-P118, ven-adaparib, BYK204165, AG14361, E7449, AZD-2461, fluzoparib, and 1,5-isoquinolinediol were provided as 10 mM stocks in DMSO from the SciLifeLab Compound Center (refer to Table S2). Bisbenzimide H 33342 trihydrochloride (Hoechst 33342, Thermo Fisher Scientific) was dissolved in MilliQ water to a stock of 20 mg/ml.

Recombinant DNA cloning

PARP2 L269A was subcloned (Table S1) from pENTR1a-PARP2 L269A-GFP (6, 17) into pENTR1a-C-mCherry by flanking SalI/NotI restriction sites and subsequently transferred to pLenti CMV Hygromycin DEST (Addgene plasmid #17454) or Ef1a-Tta3G-P2A-Blast (50). pENTR1a-PARP1 L713F-C-GFP was transferred to pLenti CMV Blast DEST (Addgene plasmid #17451).

shRNA HPF1#1, #2 and #3, and NT (nontargeting) were oligo annealed into a prSITEP-TetR-Neomycin-akaLuc. The shRNA system, backbone of the pRSITEP-U6Tet-(sh)-EF1-TetRep-2A-Puro-P2A-RFP670 plasmid (51) was modified to include a Tet-repressor for controlled shRNA expression *via* doxycycline, a neomycin resistance gene for antibiotic selection, and a luminescent reporter, akaLuc. The entire sequence is transferable using XbaI/SalI restriction sites. All subcloning into entry vectors was validated by automated sequencing; while shuttling into destination vectors was performed with Gateway LR Clonase II (Thermo Fisher Scientific) and positive clones were confirmed by colony PCR. All plasmids, synthetic genes, and primers (Eurofins Genomics) are listed in Table S1.

Lentivirus production and transduction

Lentiviral production was performed following transfection of third generation lentiviral packing vectors by calcium phosphate precipitation. prSITEP Neo, pLenti CMV Hygro, pLenti CMV Blast, or pLenti CMV Puro lentiviral constructs were cotransfected with lentiviral packaging vectors (Gag-Pol, Rev, and VSV-G envelope) into subconfluent HEK293T cells. Viral particles were harvested at 48- and 72-h post transfection, and target cells were transduced at 1:1 dilution of lentivirus and fresh, complete medium in the presence of polybrene (8 µg/ml). Forty-eight hours post transduction, target cells were replated at low density in the presence of G418/neomycin (Sigma-Aldrich, 450 µg/ml for 6 days; pIN-DUCER20–Addgene plasmid #44012), puromycin (Sigma-Aldrich, 1 µg/ml for 3 days; pLenti CMV Puro–Addgene plasmid #17452), blasticidin (Sigma-Aldrich, 5 µg/ml for 4 days; pLenti CMV Blast–Addgene plasmid #17451), or hygromycin (Sigma-Aldrich, 100 µg/ml for 5 days; pLenti CMV Hygro–Addgene plasmid #17454) that was replenished at 3-day intervals.

Reverse transcription quantitative PCR

U-2 OS cells were plated at 60,000 cells/well in 6-well plates in the absence or presence of 0.75 µg/ml doxycycline. After 72 h, the cells were harvested with TRIzol (Thermo Fisher Scientific). RNA was purified with the Direct-zol RNA Mini-Prep kit (Zymo Research) according to the manufacturer's instructions and quantified on a DeNovix DS-11 FX Spectrophotometer/Fluorometer. Complementary DNA (cDNA) was then generated with the iScript cDNA Synthesis Kit (Bio-Rad) according to the manufacturer's instructions. Quantitative PCR was performed with 2.5 ng cDNA per sample and iTaq Universal SYBR Green Supermix (Bio-Rad) using a Bio-Rad CFX96 Real-Time PCR Detection System. Relative quantity

of target genes was calculated using the $\Delta\Delta$Ct method *via* normalization to *β-actin*. All quantitative PCR primers are listed in Table S1 and were ordered from Eurofins.

Western blotting

Cells were collected by trypsinization and lysed in radio-immunoprecipitation assay buffer (20 min on ice with occasional mixing), and the clarified lysate was supplemented with Laemmli buffer (1x final). Following heating for 5 min at 95 °C, the samples were either directly loaded for electrophoresis or frozen at −20 °C for later use. Protein samples were separated on 4 to 20% gradient Mini-PROTEAN or Criterion TGX gels (Bio-Rad) prior to transferring onto 0.2 μm nitrocellulose with a Trans-Blot Turbo Transfer System (Bio-Rad). After blocking with ROTIBlock (Carl Roth) for 1 h at room temperature primary antibodies were applied in 1x ROTIStock TBST (Carl Roth) at specified concentrations and left to incubate on a shaker at 4 °C overnight. The primary antibodies used included anti-GFP probe (mouse monoclonal, 1:500; specificity confirmed by induction of transgene), anti-mCherry (rabbit polyclonal, 1:2000; specificity confirmed by induction of transgene), anti-PARP1 (mouse monoclonal, 1:500; specificity confirmed by induction of transgene), anti-PARP2 (rabbit polyclonal, 1:2000; specificity confirmed by induction of transgene), anti-GAPDH (rabbit, 1:2500), anti-β-actin (mouse monoclonal, 1:5000), and anti-HPF1 (rabbit, 1:1000; specificity confirmed by shRNA). LI-COR secondary antibodies were diluted in 1x ROTIStock TBST (Carl Roth) at 1:10,000 and incubated at room temperature for one hour. The blots were then imaged using a LI-COR Odyssey Fc system and analyzed with Image Studio Software (LI-COR, https://www.licorbio.com/image-studio). Band densities were quantified using the rectangular selection tool and median background levels with border width set to 3.

Live-cell fluorescence microscopy

For PARP L713F and PARP2 L269A experiments in live U-2 OS cells, 4000 cells were plated in transparent, clear bottom 96-well plates (BD Falcon) on day 0 in complete medium. The following day medium was changed to complete DMEM phenol-free medium, and inhibitors were added to their indicated final concentrations in complete DMEM phenol-free medium (final DMSO 0.1% or 1% [3-AB] v/v). After 16 or 24 h, cell-permeable Hoechst 33342 was added to a final concentration of 1 μg/ml for 30 min prior to imaging.

For shHPF1 experiments in live U-2 OS cells, 0.75 μg/ml doxycycline was added 72 h prior the start of the experiment. After this period, cells were trypsinized and 4000 cells were plated in transparent, clear bottom 96-well plates (BD Falcon) on day 0 in DMEM phenol-free medium. The next day, inhibitors were added to their indicated final concentrations in complete DMEM phenol-free medium (final DMSO 0.1% or 1% [3-AB] v/v). After 24 h, cell-permeable Hoechst 33342 was added to a final concentration of 1 μg/ml for 30 min prior to imaging.

Imaging was performed using the CELLCYTE X microscope (CYTENA) at 10x magnification. The microscope was maintained at 37 °C with 5% CO_2 in a humidified incubator. Image analysis was then performed with CellProfiler software (Broad Institute, https://cellprofiler.org) where the mean nuclei intensity upper quartile intensity mask of both GFP and mCherry were used to understand the fold changes and the integrated Hoechst intensity was used for cell cycle analysis.

For PARP L713F and PARP2 L269A time course experiment in live U-2 OS cells, 6000 cells were plated in transparent, clear bottom 96-well plates (BD Falcon) on day 0 in complete medium. The following day medium was changed to complete DMEM phenol-free medium, and inhibitors were added to their indicated final concentrations in complete DMEM phenol-free medium (final 0.1% DMSO [v/v]). Imaging was performed every 2 h for 26 h using an IncuCyte S3 (Sartorius) at 20x magnification. Image analysis was performed with CellProfiler software as above.

Small molecule screen details

Composition, storage, and plating of screened compounds

Hit molecules from an earlier PARP1 L713F stability screen ([17]) were handled and plated as before but into clear 96-well cell culture plates (Sarstedt) using an Echo 550 acoustic liquid handler (LabCyte). An overview of the small molecules screened is detailed in Table S2.

Screen execution

U-2 OS PARP1 L713F-GFP/PARP2 L269A-mCherry cells were plated at 10,000 cells per well into drug-containing assay plates (final concentration 10 μM) using a Multidrop Combi liquid dispenser (Thermo Fisher Scientific). Cells were then incubated with drugs for 16 h at 37 °C with 5% CO_2 in a humidified incubator. To minimize edge effects, the plates were placed in self-made humidity chambers that limited evaporation in the outer ring of wells. Imaging was performed using the CELLCYTE X microscope (CYTENA) at 10x magnification. The microscope was maintained at 37 °C with 5% CO_2 in a humidified incubator. Image analysis was then performed with CellProfiler software (Broad Institute) where the mean nuclei intensity upper quartile intensity mask of both GFP and mCherry were used to understand the fold changes. The same strategy was applied to measure the concentration-curves of all the non-PARPi (DC-05, A-395, ACY-1083, droxinostat, KDM5-C70, bisindolylmaleimide I [GF109203X], AZ960, Go 6983, linifanib [ABT-869], paclitaxel, PF-3758309, AT9283, azacitidine, and decitabine).

Cellular thermal shift assay

CCRF-CEM cells (1×10^6 per treatment) were harvested by centrifugation at 500*g* for 5 min and washed twice with PBS. Post washing, cells were resuspended in 4 ml Tris-buffered saline containing a cocktail of proteasome inhibitors (EDTA-free, Roche). Cell lysis was achieved by alternately exposing cells to dry ice and absolute ethanol for 3 min and to a temperature of 37 °C for 3 min, repeating this cycle three times.

Subsequently, lysates were centrifuged at 20,000*g* for 20 min at 4 °C. The supernatant was collected and aliquoted into 100 μl fractions. Each aliquot was treated with either DMSO or 10 μM olaparib and incubated at room temperature for 20 min. Thermal denaturation was conducted at a range of temperatures: 37 °C, 40 °C, 43 °C, 46 °C, 49 °C, 52 °C, 55 °C, 58 °C, 61 °C, 64 °C, 67 °C, and 70 °C, each for 3 min. Samples were then cooled down at room temperature for 3 min before being centrifuged at 20,000*g* for 20 min at 4 °C. Samples were prepared by adding Laemmli 4X sample buffer and heated to 95 °C for complete denaturation. Proteins were then resolved by SDS-PAGE and transferred onto membranes for Western blot analysis, as above.

U-2 OS PARP1 L713F-GFP/PARP2 L269A-mCherry cells (1 x 10⁶ per treatment) were harvested by trypsinization followed by 2x PBS wash by centrifugation at 500*g* for 5 min. Cells were resuspended in Tris-buffered saline containing a cocktail of proteasome inhibitors and frozen at −80 °C for later use. Cell lysis was performed as above, and supernatant of centrifuged cell lysate was aliquoted into 350 μl fractions. Each aliquot was treated with either DMSO, 100 nM talazoparib, 20 μM talazoparib, 100 nM AZD5305, or 20 μM AZD5305 and incubated at room temperature for 25 min. Thermal denaturation was done at the temperatures: 37 °C, 46 °C, 53 °C, 58 °C, and 68 °C, each for 3 min. Samples were then cooled to room temperature, centrifuged, and prepared for Western blot analysis as above.

Immunofluorescence microscopy

U-2 OS cells were seeded at a density of 4000 cells per well in a PhenoPlate 96-well plate (PerkinElmer). The next day, DMSO (0.1% v/v, final) or 10 μM bisindolylmaleimide I (GF109203X) was added to each well. After 24 h, the cells were fixed with 4% paraformaldehyde (Histolab) for 15 min and then permeabilized with 0.1% Triton X-100 (Sigma-Aldrich) in PBS for 15 min. Afterward, the cells were blocked with 2% bovine serum albumin (BSA, Sigma-Aldrich) in PBS for one hour at room temperature. The cells were then incubated with a primary anti-PARP1 recombinant antibody (rabbit recombinant; specificity confirmed with secondary only controls) diluted 1:200 in 0.1% BSA in PBS, for 2 h at room temperature. Alexa Fluor 568- and Alexa Fluor 488-conjugated secondary antibodies (anti-rabbit) were diluted 1:500 in 0.1% BSA in PBS and incubated at room temperature in the dark. After secondary incubation, cells were stained with Hoechst at a 1:2000 dilution for 5 min at room temperature. Cells were imaged using a A1R + Nikon confocal microscope system at 20x magnification. The 568-channel spectral free band (VF) ranged between 590 and 620 nm and the 488-channel spectral free band (VF) ranged between 490 to 530 nm.

Statistical analysis

All graphing and statistical analyses were performed using GraphPad Prism V10 (https://www.graphpad.com/features) or R Studio v4.1.1. Saturation curve fitting was performed using the [agonist] versus response four parameter variable slope

model in GraphPad Prism. Specific *post hoc* tests, variations, and statistical significances for relevant experiments are described within individual figure legends. For Tables 3 and 4 the logEC$_{50}$ *p* values were measured using unpaired, two-tailed *t* test assuming both populations have the same SD (standard deviation).

Data availability

All data are available in the main text and in supporting information. Materials are available from the corresponding authors (Nicholas Valerie – nicholas.valerie@ki.se; Mikael Altun – mikael.altun@ki.se) upon reasonable request.

PARP inhibitor selectivity profiling in cells with CeTEAM

DNA; CeTEAM, cellular target engagement by accumulation of mutant; CETSA, cellular thermal shift assay; DMEM, Dulbecco's modified Eagle medium; DMSO, dimethyl sulfoxide; FBS, fetal bovine serum; HD, helical domain; HPF, histone PARylation factor 1; MDS, multidimensional scaling; PARP, Poly (ADP-ribose) polymerase; PARPi, PARP inhibitor; PAR, poly (ADP-ribose).

References

1. Lord, C. J., and Ashworth, A. (2017) PARP inhibitors: synthetic lethality in the clinic. *Science* **355**, 1152–1158

2. Bryant, H. E., Schultz, N., Thomas, H. D., Parker, K. M., Flower, D., Lopez, E., *et al.* (2005) Specific killing of BRCA2-deficient tumours with inhibitors of poly(ADP-ribose) polymerase. *Nature* **434**, 913–917

3. Farmer, H., McCabe, N., Lord, C. J., Tutt, A. N., Johnson, D. A., Richardson, T. B., *et al.* (2005) Targeting the DNA repair defect in BRCA mutant cells as a therapeutic strategy. *Nature* **434**, 917–921

4. Thorsell, A. G., Ekblad, T., Karlberg, T., Löw, M., Pinto, A. F., Trésaugues, L., *et al.* (2017) Structural basis for potency and promiscuity in poly(ADP-ribose) polymerase (PARP) and tankyrase inhibitors. *J. Med. Chem.* **60**, 1262–1271

5. Rudolph, J., Jung, K., and Luger, K. (2022) Inhibitors of PARP: number crunching and structure gazing. *Proc. Natl. Acad. Sci. U. S. A* **119**, e2121979119

6. Langelier, M. F., Riccio, A. A., and Pascal, J. M. (2014) PARP-2 and PARP-3 are selectively activated by 5' phosphorylated DNA breaks through an allosteric regulatory mechanism shared with PARP-1. *Nucleic Acids Res.* **42**, 7762–7775

7. Rouleau-Turcotte, É., and Pascal, J. M. (2023) ADP-ribose contributions to genome stability, and PARP enzyme trapping on sites of DNA damage; paradigm shifts for a coming-of-age modification. *J. Biol. Chem.* **299**, 105397

8. Bai, P. (2015) Biology of poly(ADP-ribose) polymerases: the factotums of cell maintenance. *Mol. Cell* **58**, 947–958

9. LaFargue, C. J., Dal Molin, G. Z., Sood, A. K., and Coleman, R. L. (2019) Exploring and comparing adverse events between PARP inhibitors. *Lancet Oncol.* **20**, e15–e28

10. Farrés, J., Llacuna, L., Martin-Caballero, J., Martínez, C., Lozano, J. J., Ampurdanés, C., *et al.* (2015) PARP-2 sustains erythropoiesis in mice by limiting replicative stress in erythroid progenitors. *Cell Death Differ.* **22**, 1144–1157

11. Vasta, J. D., Corona, C. R., Wilkinson, J., Zimprich, C. A., Hartnett, J. R., Ingold, M. R., *et al.* (2018) Quantitative, wide-spectrum kinase profiling in live cells for assessing the effect of cellular ATP on target engagement *cell. Chem. Biol.* **25**, 206–214.e211

12. Suskiewicz, M. J., Zobel, F., Ogden, T. E. H., Fontana, P., Ariza, A., Yang, J. C., *et al.* (2020) HPF1 completes the PARP active site for DNA damage-induced ADP-ribosylation. *Nature* **579**, 598–602

13. Gibbs-Seymour, I., Fontana, P., Rack, J. G. M., and Ahel, I. (2016) HPF1/C4orf27 is a PARP-1-interacting protein that regulates PARP-1 ADP-ribosylation activity. *Mol. Cell* **62**, 432–442

14. Stojanovic, P., Luger, K., and Rudolph, J. (2023) Slow dissociation from the PARP1-HPF1 complex drives inhibitor potency. *Biochemistry* **62**, 2382–2390

15. Rudolph, J., Roberts, G., and Luger, K. (2021) Histone Parylation factor 1 contributes to the inhibition of PARP1 by cancer drugs. *Nat. Commun.* **12**, 736

16. Prokhorova, E., Zobel, F., Smith, R., Zentout, S., Gibbs-Seymour, I., Schützenhofer, K., *et al.* (2021) Serine-linked PARP1 auto-modification controls PARP inhibitor response. *Nat. Commun.* **12**, 4055

17. Valerie, N. C. K., Sanjiv, K., Mortusewicz, O., Zhang, S. M., Alam, S., Pires, M. J., *et al.* (2024) Coupling cellular drug-target engagement to downstream pharmacology with CeTEAM. *Nat. Commun.* **15**, 10347

18. Burtscher, M. L., Gade, S., Garrido-Rodriguez, M., Rutkowska, A., Werner, T., Eberl, H. C., *et al.* (2024) Network integration of thermal proteome profiling with multi-omics data decodes PARP inhibition. *Mol. Syst. Biol.* **20**, 458–474

19. Knezevic, C. E., Wright, G., Rix, L. L. R., Kim, W., Kuenzi, B. M., Luo, Y., *et al.* (2016) Proteome-wide profiling of clinical PARP inhibitors reveals compound-specific secondary targets. *Cell Chem. Biol.* **23**, 1490–1503

20. Howard, R. T., Hemsley, P., Petteruti, P., Saunders, C. N., Molina Bermejo, J. A., Scott, J. S., *et al.* (2020) Structure-guided Design and in-cell target profiling of a cell-active target engagement probe for PARP inhibitors. *ACS Chem. Biol.* **15**, 325–333

21. Shaw, J., Dale, I., Hemsley, P., Leach, L., Dekki, N., Orme, J. P., *et al.* (2019) Positioning high-throughput CETSA in early drug discovery through screening against B-raf and PARP1. *SLAS Discov.* **24**, 121–132

22. Martinez Molina, D., Jafari, R., Ignatushchenko, M., Seki, T., Larsson, E. A., Dan, C., *et al.* (2013) Monitoring drug target engagement in cells and tissues using the cellular thermal shift assay. *Science* **341**, 84–87

23. Langelier, M. F., Lin, X., Zha, S., and Pascal, J. M. (2023) Clinical PARP inhibitors allosterically induce PARP2 retention on DNA. *Sci. Adv.* **9**, eadf7175

24. Tomassi, S., Pfahler, J., Mautone, N., Rovere, A., Esposito, C., Passeri, D., *et al.* (2020) From PARP1 to TNKS2 inhibition: a structure-based approach. *ACS Med. Chem. Lett.* **11**, 862–868

25. Illuzzi, G., Staniszewska, A. D., Gill, S. J., Pike, A., McWilliams, L., Critchlow, S. E., *et al.* (2022) Preclinical characterization of AZD5305, A next-generation, highly selective PARP1 inhibitor and trapper. *Clin. Cancer Res.* **28**, 4724–4736

26. Johannes, J. W., Balazs, A., Barratt, D., Bista, M., Chuba, M. D., Cosulich, S., *et al.* (2021) Discovery of 5-{4-[(7-Ethyl-6-oxo-5,6-dihydro-1,5-naphthyridin-3-yl)methyl]piperazin-1-yl}. *J. Med. Chem.* **64**, 14498–14512

27. Tamir, T. Y., Drewry, D. H., Wells, C., Major, M. B., and Axtman, A. D. (2020) PKIS deep dive yields a chemical starting point for dark kinases and a cell active BRSK2 inhibitor. *Sci. Rep.* **10**, 15826

28. Buchstaller, H. P., Anlauf, U., Dorsch, D., Kuhn, D., Lehmann, M., Leuthner, B., *et al.* (2019) Discovery and optimization of 2-Arylquinazolin-4-ones into a potent and selective tankyrase inhibitor modulating wnt pathway activity. *J. Med. Chem.* **62**, 7897–7909

29. Lindgren, A. E., Karlberg, T., Thorsell, A. G., Hesse, M., Spjut, S., Ekblad, T., *et al.* (2013) PARP inhibitor with selectivity toward ADP-ribosyltransferase ARTD3/PARP3. *ACS Chem. Biol.* **8**, 1698–1703

30. Cai, S. X., Ma, N., Wang, X., Guo, M., Jiang, Y., and Tian, Y. E. (2024) The discovery of a potent PARP1 inhibitor Senaparib. *Mol. Cancer Ther.* **24**, 47–55

31. Lee, M., Je, I. G., Kim, J. E., Yoo, Y., Lim, J. H., Jang, E., *et al.* (2023) Venadaparib is a novel and selective PARP inhibitor with improved physicochemical properties, efficacy, and safety. *Mol. Cancer Ther.* **22**, 333–342

32. Papeo, G., Posteri, H., Borghi, D., Busel, A. A., Caprera, F., Casale, E., *et al.* (2015) Discovery of 2-[1-(4,4-Difluorocyclohexyl)piperidin-4-yl]-6-fluoro-3-oxo-2,3-dihydro-1H-isoindole-4-carboxamide (nms-P118): a potent, orally available, and highly selective PARP-1 inhibitor for cancer therapy. *J. Med. Chem.* **58**, 6875–6898

33. Murai, J., Huang, S. Y., Das, B. B., Renaud, A., Zhang, Y., Doroshow, J. H., *et al.* (2012) Trapping of PARP1 and PARP2 by clinical PARP inhibitors. *Cancer Res.* **72**, 5588–5599

34. Michelena, J., Lezaja, A., Teloni, F., Schmid, T., Imhof, R., and Altmeyer, M. (2018) Analysis of PARP inhibitor toxicity by multidimensional fluorescence microscopy reveals mechanisms of sensitivity and resistance. *Nat. Commun.* **9**, 2678

35. Holdgate, G. A., Meek, T. D., and Grimley, R. L. (2018) Mechanistic enzymology in drug discovery: a fresh perspective. *Nat. Rev. Drug Discov.* **17**, 115–132

36. Jones, P., Altamura, S., Boueres, J., Ferrigno, F., Fonsi, M., Giomini, C., *et al.* (2009) Discovery of 2-{4-[(3S)-piperidin-3-yl]phenyl}-2H-indazole-7-carboxamide (MK-4827): a novel oral poly(ADP-ribose)polymerase (PARP) inhibitor efficacious in BRCA-1 and -2 mutant tumors. *J. Med. Chem.* **52**, 7170–7185

37. Backman, T. W., Cao, Y., and Girke, T. (2011) ChemMine tools: an online service for analyzing and clustering small molecules. *Nucleic Acids Res.* **39**, W486–W491

38. Langelier, M. F., Billur, R., Sverzhinsky, A., Black, B. E., and Pascal, J. M. (2021) HPF1 dynamically controls the PARP1/2 balance between

initiating and elongating ADP-ribose modifications. *Nat. Commun.* **12**, 6675

39. Zentout, S., Imburchia, V., Chapuis, C., Duma, L., Schützenhofer, K., Prokhorova, E., *et al.* (2024) Histone ADP-ribosylation promotes resistance to PARP inhibitors by facilitating PARP1 release from DNA lesions. *Proc. Natl. Acad. Sci. U. S. A* **121**, e2322689121

40. Wu, X., Liu, J., Wang, J., Wang, L., Lin, Z., Wang, X., *et al.* (2024) Senaparib as first-line maintenance therapy in advanced ovarian cancer: a randomized phase 3 trial. *Nat. Med.* **30**, 1612–1621

41. Zhao, H., Ji, M., Cui, G., Zhou, J., Lai, F., Chen, X., *et al.* (2017) Discovery of novel quinazoline-2,4(1H,3H)-dione derivatives as potent PARP-2 selective inhibitors. *Bioorg. Med. Chem.* **25**, 4045–4054

42. [preprint] Smith-Pillet, E. S., Billur, R., Langelier, M. F., Talele, T. T., Pascal, J. M., and Black, B. E. (2024) A PARP2-specific active site α-helix melts to permit DNA damage-induced enzymatic activation. *bioRxiv.* https://doi.org/10.1101/2024.05.20.594972

43. Xue, H., Bhardwaj, A., Yin, Y., Fijen, C., Ephstein, A., Zhang, L., *et al.* (2022) A two-step mechanism governing PARP1-DNA retention by PARP inhibitors. *Sci. Adv.* **8**, eabq0414

44. Zandarashvili, L., Langelier, M. F., Velagapudi, U. K., Hancock, M. A., Steffen, J. D., Billur, R., *et al.* (2020) Structural basis for allosteric PARP-1 retention on DNA breaks. *Science* **368**, eaax6367

45. Yuan, Y., Liao, Y. M., Hsueh, C. T., and Mirshahidi, H. R. (2011) Novel targeted therapeutics: inhibitors of MDM2, ALK and PARP. *J. Hematol. Oncol.* **4**, 16

46. Bedikian, A. Y., Papadopoulos, N. E., Kim, K. B., Hwu, W. J., Homsi, J., Glass, M. R., *et al.* (2009) A phase IB trial of intravenous INO-1001 plus oral temozolomide in subjects with unresectable stage-III or IV melanoma. *Cancer Invest.* **27**, 756–763

47. Morrow, D. A., Brickman, C. M., Murphy, S. A., Baran, K., Krakover, R., Dauerman, H., *et al.* (2009) A randomized, placebo-controlled trial to evaluate the tolerability, safety, pharmacokinetics, and pharmacodynamics of a potent inhibitor of poly(ADP-ribose) polymerase (INO-1001) in patients with ST-elevation myocardial infarction undergoing primary percutaneous coronary intervention: results of the TIMI 37 trial. *J. Thromb. Thrombolysis* **27**, 359–364

48. Langelier, M. F., Planck, J. L., Roy, S., and Pascal, J. M. (2012) Structural basis for DNA damage-dependent poly(ADP-ribosyl)ation by human PARP-1. *Science* **336**, 728–732

49. Dawicki-McKenna, J. M., Langelier, M. F., DeNizio, J. E., Riccio, A. A., Cao, C. D., Karch, K. R., *et al.* (2015) PARP-1 activation requires local unfolding of an autoinhibitory domain. *Mol. Cell* **60**, 755–768

50. Kanellis, D. C., Espinoza, J. A., Zisi, A., Sakkas, E., Bartkova, J., Katsori, A. M., *et al.* (2021) The exon-junction complex helicase eIF4A3 controls cell fate via coordinated regulation of ribosome biogenesis and translational output. *Sci. Adv.* **7**, eabf7561

51. Eshtad, S., Mavajian, Z., Rudd, S. G., Visnes, T., Boström, J., Altun, M., *et al.* (2016) hMYH and hMTH1 cooperate for survival in mismatch repair defective T-cell acute lymphoblastic leukemia. *Oncogenesis* **5**, e275